

PHYSICS

Tunable Weyl and Dirac states in the nonsymmorphic compound CeSbTe

Leslie M. Schoop,^{1*} Andreas Topp,¹ Judith Lippmann,¹ Fabio Orlandi,² Lukas Mühler,³ Maia G. Vergniory,^{4,5} Yan Sun,⁶ Andreas W. Rost,^{1,7†} Viola Duppel,¹ Maxim Krivenkov,⁸ Shweta Sheoran,¹ Pascal Manuel,² Andrei Varykhalov,⁸ Binghai Yan,⁹ Reinhard K. Kremer,¹ Christian R. Ast,¹ Bettina V. Lotsch^{1,10,11}

Recent interest in topological semimetals has led to the proposal of many new topological phases that can be realized in real materials. Next to Dirac and Weyl systems, these include more exotic phases based on manifold band degeneracies in the bulk electronic structure. The exotic states in topological semimetals are usually protected by some sort of crystal symmetry, and the introduction of magnetic order can influence these states by breaking time-reversal symmetry. We show that we can realize a rich variety of different topological semimetal states in a single material, CeSbTe. This compound can exhibit different types of magnetic order that can be accessed easily by applying a small field. Therefore, it allows for tuning the electronic structure and can drive it through a manifold of topologically distinct phases, such as the first nonsymmorphic magnetic topological phase with an eightfold band crossing at a high-symmetry point. Our experimental results are backed by a full magnetic group theory analysis and *ab initio* calculations. This discovery introduces a realistic and promising platform for studying the interplay of magnetism and topology. We also show that we can generally expand the numbers of space groups that allow for high-order band degeneracies by introducing antiferromagnetic order.

INTRODUCTION

In recent years, the field of topological semimetals has flourished because of the discovery of many materials that exhibit highly exotic physical properties that are a result of massless quasi-particles, which dominate the transport properties (1–3). For example, three-dimensional Dirac semimetals (3D DSMs) and Weyl semimetals (WSMs) have been shown to host unusual electronic transport properties, as evidenced by their ultrahigh carrier mobility, their extremely large magnetoresistance, and indications of the chiral anomaly (4, 5). The current vast progress in the field draws the prospect of developing new spintronic devices based on topological materials closer (6). To overcome existing limitations, such as the necessity of high magnetic fields to access several topological effects, new and improved materials are of high demand. In particular, materials that exhibit long-range magnetic order in combination with topologically nontrivial band structures are sparse. However, it is exactly these types of materials that may solve present challenges for spintronic applications (7).

3D DSMs exhibit a fourfold degenerate point in their electronic structure, which is a result of a crossing of two doubly degenerate bands. If inversion symmetry (IS) or time-reversal symmetry (TRS) is broken

in a 3D DSM, then the doubly degenerate bands become spin-split, resulting in doubly degenerate band crossings called Weyl nodes (8). Although WSMs have been established for some time through IS breaking (9, 10), there are only very few examples of TRS breaking WSMs, examples of which are GdPtBi or cobalt-based Heusler alloys (11, 12). Antiferromagnetic (AFM) DSMs are even found more rarely, one example being CuMnAs (13, 14), where it has been shown that although TRS and IS are broken individually, the product of both still holds, which leads to fourfold degenerate Dirac cones in its AFM structure. Contrary to most 3D DSMs and WSMs, where the band degeneracy is dependent on the orbital character of the bands, materials that crystallize in nonsymmorphic space groups exhibit band degeneracies that are imposed by the space group symmetry (15–17). These degeneracies are guaranteed to be present if a nonsymmorphic symmetry operation relates atoms in the crystal structure and thus predictions on topological features can be solely based on group theory in these cases. This concept has been used to predict DSMs and completely new quasi-particles (the so-called new fermions), beyond Dirac, Weyl, or Majorana fermions (16, 17). These (yet to be discovered) new fermions are not constrained by Poincaré symmetry, only exist in the solid state, and have no high-energy counterparts (16). Their unusual Landau-level structure distinguishes them from normal Weyl points. The concept of creating these new quasi-particles is based on the possibility of achieving three-, six-, or eightfold band degeneracies in nonsymmorphic space groups. However, whether these degeneracies appear at the Fermi level depends on the electron filling, which complicates the search for these topological semimetals (18, 19). To date, only very few materials have been experimentally shown to exhibit bulk band degeneracies protected by nonsymmorphic symmetry, examples of which are ZrSiS and ZrSiTe (19–21). It has also not yet been studied experimentally how magnetism and, thus, TRS breaking affect the band degeneracies that result from nonsymmorphic symmetry, mostly due to a lack of these candidate materials [but a theoretical classification of degeneracies in magnetic groups has recently been performed (22)]. A magnetic nonsymmorphic compound could be a new type of magnetic WSM

Copyright © 2018
The Authors, some
rights reserved;
exclusive licensee
American Association
for the Advancement
of Science. No claim to
original U.S. Government
Works. Distributed
under a Creative
Commons Attribution
NonCommercial
License 4.0 (CC BY-NC).

¹Max-Planck-Institut für Festkörperforschung, Heisenbergstraße 1, D-70569 Stuttgart, Germany. ²ISIS Neutron Pulsed Facility, Science and Technology Facilities Council, Rutherford Appleton Laboratory, Oxford OX11 0QX, UK. ³Department of Chemistry, Princeton University, Princeton, NJ 08544, USA. ⁴Donostia International Physics Center, Paseo Manuel de Lardizabal 4, 20018 Donostia-San Sebastian, Spain. ⁵Ikerbasque, Basque Foundation for Science, E-48011 Bilbao, Spain. ⁶Max-Planck-Institut für Chemische Physik fester Stoffe, 01187 Dresden, Germany. ⁷Physikalisches Institut, Universität Stuttgart, Pfaffenwaldring 57, 70569 Stuttgart, Germany. ⁸Elektronenspeicherring BESSY II, Helmholtz-Zentrum Berlin für Materialien und Energie, Albert-Einstein-Straße 15, 12489 Berlin, Germany. ⁹Department of Condensed Matter Physics, Weizmann Institute of Science, Rehovot 76100, Israel. ¹⁰Department of Chemistry, Ludwig-Maximilians-Universität München, Butenandtstr. 5-13, 81377 München, Germany. ¹¹Nanosystems Initiative Munich and Center for Nanoscience, Schellingstrasse 4, 80799 München, Germany.

*Corresponding author. Email: lschoop@princeton.edu

†Present address: Scottish Universities Physics Alliance, School of Physics and Astronomy, University of St Andrews, North Haugh, St Andrews, Fife KY16 9SS, UK.

that combines long-range magnetic order with new quasi-particles. In addition, not only does antiferromagnetic order affect TRS, but it can also break or induce further symmetry elements. It has not yet been studied how this influences band structures that are governed by nonsymmorphic symmetry.

In times where many topological materials have been realized, the challenge to introduce compounds that combine several different states in a single material and allow for switching between these different topological states remains. Here, we show that the compound CeSbTe exhibits Dirac and Weyl fermions and that both types, nonsymmorphically protected and accidental band crossings, are present in the vicinity of the Fermi level. We also show that this material can exhibit more exotic three- and eightfold degeneracies. Although CeSbTe is centrosymmetric, TRS can be broken by applying a very small magnetic field. CeSbTe orders antiferromagnetically below $T_N = 2.7$ K at zero field but undergoes a metamagnetic transition to a fully polarized state under a small field of about 0.25 T. This magnetically fully polarized state with ferromagnetic (FM)-like polarization will be, for simplicity, referred to as FM phase within this manuscript. We show with detailed magnetic measurements combined with ab initio calculations and angle-resolved photoemission spectroscopy (ARPES) measurements that this material allows for easy access to a plethora of different Dirac and Weyl states, of which some have not previously been realized in a real material. Using the recently implemented double group representations (23–26), we performed a group theory analysis (16, 23–26) that supports our ab initio claims of the existence of protected Dirac and Weyl nodes, as well as three- and eightfold crossings at high-symmetry points or lines, thus presenting the first realization of a nonsymmorphic topological material that exhibits degeneracies other than fourfold ones. We also show that AFM order gives access to new fermion states in space groups that have not been previously considered.

RESULTS

Figure 1 shows a drawing of the crystal structure of CeSbTe; an image of a typical single crystal is shown in the inset. Contrary to a previous study

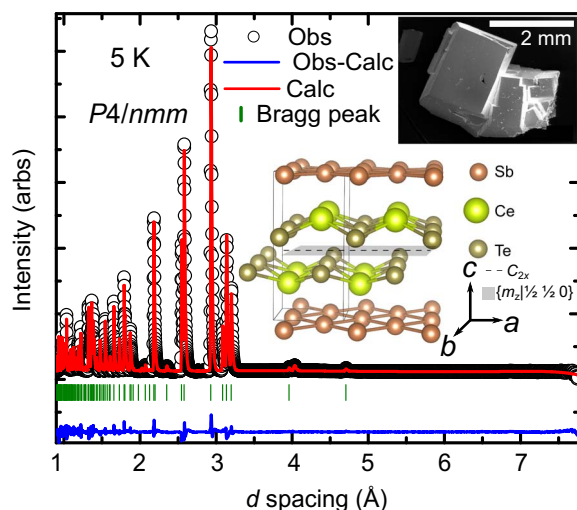


Fig. 1. Refined neutron diffraction data taken at 5 K. Small impurity peaks were excluded from the refinement. The upper inset shows a scanning electron microscopy image of a typical crystal of CeSbTe, and the lower inset shows a drawing of the crystal structure of CeSbTe, where the nonsymmorphic symmetry elements are highlighted. arbs, arbitrary units; Obs, observed; Calc, calculated.

(27), which reported that CeSbTe crystallized in the orthorhombic space group $Pnma$ (no. 62), we found that it crystallizes in the tetragonal space group $P4/nmm$ (no. 129), as evidenced by the refined neutron diffraction data (Fig. 1). Single-crystal x-ray diffraction (SXRD) and precession electron diffraction (PED) yielded the same result (see the Supplementary Materials for details). With PED, we did not detect any of the additional reflections that would be expected for space group $Pnma$ (fig. S1). Thus, CeSbTe is an isostructural and isoelectronic version of the nodal line semimetal ZrSiS (20, 28). The crystal structure is composed of CeTe bilayers that are separated by a square-net layer of Sb; the layers stack along c (see the inset of Fig. 1). The Ce atoms form a square network arrangement, and the intralayer distance of Ce atoms is 4.37 Å, whereas the interlayer distance is 5.26 Å within a bilayer and 6.02 Å across a bilayer. ZrSiS and related compounds have been shown to exhibit a diamond-shaped Dirac line node and fourfold degenerate nodes at the X, R, M, and A points of the Brillouin zone (BZ) (20, 21). The latter ones are a result of the nonsymmorphic glide planes in the space group $P4/nmm$, and the resulting Dirac cones and nodes have been discussed and illustrated many times (21, 29). Although the Dirac line node is gapped by spin-orbit coupling (SOC), the degeneracies that result from nonsymmorphic symmetry are not affected by SOC. The nonsymmorphic degeneracies can be above, below, or right at the Fermi level, depending on the c/a ratio of the lattice constants (19). For further information on the crystal structure and sample quality, see high-resolution transmission electron microscopy images with atomic resolution in the Supplementary Materials.

The clarification of the crystal structure allows us to calculate the electronic band structure, to find out whether the system is not only structurally but also electronically similar to ZrSiS and related nonsymmorphic Dirac materials. A close-up of the calculated electronic structure, without considering magnetic order, can be found in Fig. 2A, showing the expected nonsymmorphically protected fourfold degeneracies at M (all crossings in the figure are protected by the nonsymmorphic symmetry), and a more detailed discussion will follow later in the paper. Because density functional theory (DFT) on f electron systems has been proven to be challenging, we performed ARPES measurements on the paramagnetic phase (samples were measured at room temperature without a magnetic field) to qualitatively confirm the predicted electronic structure. Because we measured at a fixed photon energy and thus cannot be certain about the k_z position we are probing, we chose the FM direction to compare measured and predicted bands, because the electronic structure is more 2D, that is, has less k_z dispersion along this direction, in contrast to other cuts that are shown in the Supplementary Materials. This can be seen in Fig. 2A, where the calculated bands along $\Gamma M \Gamma$ and ZAZ are plotted in one diagram. Figure 2B shows the measured dispersion along $\Gamma M \Gamma$. Almost all bands are clearly resolved in the measurement. Some bulk bands are not visible, which we attribute to matrix element effects (see the Supplementary Materials for more ARPES data along different high-symmetry lines). To get a better understanding of the discrepancies between prediction and measurement, we extracted the intensity maxima from the measured data and show them in red circles on top of the data in Fig. 2C. We additionally performed a surface state calculation, as shown in Fig. 2D. The red bands indicate surface-derived states, which are commonly observed in ZrSiS-type materials, and are a result of the loss of nonsymmorphic symmetry at the surface (29). A comparison between the surface calculation and the measured data clearly shows an agreement between experiment and DFT. Thus, DFT gives a qualitatively correct description of the electronic structure. We are

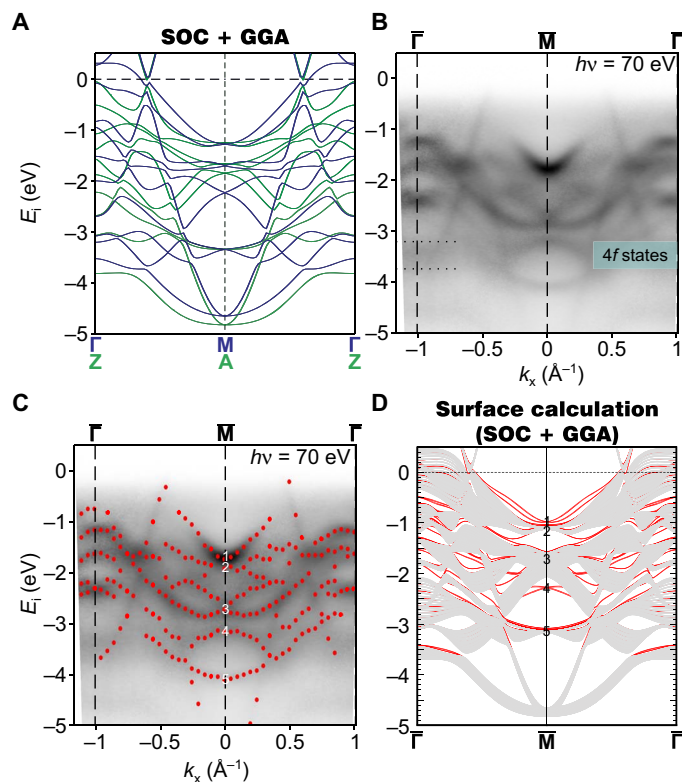


Fig. 2. Comparison of measured and calculated electronic structure of CeSbTe. (A) Calculated bulk band structure plotted along $\Gamma\text{M}\Gamma$ (blue) in comparison to ZAZ (green). Along this path, the band structure is relatively 2D. All crossings at M are forced by nonsymmorphic symmetry. (B) Dispersion along $\Gamma\text{M}\Gamma$ measured with ARPES. Except for the energy scaling, the measured band structure is in agreement with the calculations. The 4f states are highlighted in blue on the right side and with dashed lines on the left side. (C) Measured data overlaid with extracted maximal intensity data shown as red circles. The observed crossings at M are numerated. (D) Surface band structure calculation with surface-derived bands shown in red. The crossings at M are numerated analogous to the measured data.

even able to resolve some delicate features close to the Fermi level, such as a nonsymmorphic degenerate point at X (see fig. S5). We also observe a flat, nondispersive band at around 3.1 eV below the Fermi level. We attribute these states to the localized Ce $4f^1$ band, which would be expected to be around this energy in a Ce^{3+} compound that contains localized 4f states. Note that the 4f states were modeled as core states in the calculation of the paramagnetic phase but will be included for the calculation of magnetically ordered phases later in the manuscript. Here, the experimental observation of 4f states serves as a guide to match the DFT calculations to the experimental observations. The energy of the 4f band agrees well with the photoemission spectra of CeTe or CeBi (30). The localization of the 4f states is further strengthened by our magnetic susceptibility data that clearly indicate that CeSbTe contains one localized 4f electron per Ce atom. The magnetization data will be described in the following paragraph. Thus, we can conclude that, although the 4f states are responsible for the magnetism in CeSbTe, they do not interfere severely with the electronic structure beyond providing an effective exchange field in the polarized phase.

Temperature-dependent measurements of the magnetic susceptibility of a single crystal of CeSbTe are shown in Fig. 3A. The field was applied along the c axis (see the Supplementary Materials for the other field orientation). For data with low field strengths, the susceptibility

shows a sharp cusp at the Néel temperature $T_N = 2.7$ K, indicative of the emergence of AFM order below this temperature [the exact transition temperature was derived from plotting $d(\chi T)/dT$ versus T]. For field strengths larger than 0.25 T, the cusp disappears and the susceptibility continues to increase with decreasing temperature, saturating at very low temperatures, reminiscent of FM behavior (reaching the fully polarized state). Curie-Weiss fits (see the Supplementary Materials) reveal an effective moment of $2.50 \mu_B$ per formula unit, which matches the expected free ion value of $2.54 \mu_B$ for a Ce^{3+} ion well. Deviations from the Curie-Weiss law at low temperatures are due to the crystal electric field (CEF) splitting of the sixfold degenerate ground state of Ce^{3+} . Fits of the susceptibilities indicate a separation of the first excited CEF doublet of ≈ 150 K (see fig. S6B). Because we observe the expected Curie-Weiss moment of $2.50 \mu_B$ per formula unit, the magnetic order is most likely a result of a Ruderman-Kittel-Kasuya-Yosida interaction, where the conduction electrons mediate the exchange between localized spins. The observed moment also indicates that the Ce 4f states are localized and away from the Fermi level. The field-dependent data (Fig. 3B) elucidate the transition from an AFM to an FM (fully polarized) phase; at a field of $\mu_0 H_c = 0.224$ T, the field-dependent susceptibility shows a sudden increase. As shown in Fig. 3B, the required field is higher (1.75 T) if the field is applied perpendicular to the c axis, which is the usual observation for spin-flop transitions. This indicates that the moments prefer to align along the c axis (that is, the easy axis). The expected saturation moment of a Ce^{3+} ion ($1 \mu_B$ per Ce) is reached faster if the field is aligned perpendicular to the c axis. A possible explanation for this behavior is a strong magnetic anisotropy of the Ce moments. Similar field-dependent magnetic transitions have also been observed in different square lattice Ce compounds, such as CeTe₂ or CeSbSe (31, 32). Moreover, other magnetic square lattice compounds, such as CsCo₂Se₂, can show a field-induced magnetic transition (33).

The magnetic properties were additionally investigated with specific heat measurements (see Fig. 3C). At zero field, a magnetic transition is clearly visible at 2.7 K (derived from the C/T plot shown in the inset), agreeing well with the susceptibility data. Although the AFM phase transition (sharp peak in C/T) is shifted to slightly lower temperatures with a small applied field (here, the field is applied along the c axis), which is typical for AFM order, the crossover seen as a broad peak in C/T shifts to higher temperatures when the applied field is larger than 1 T, reminiscent of behavior seen in ferromagnets. The crossover between the two different types of magnetic order is therefore also reflected in the specific heat. For information about magnetic entropy, see the Supplementary Materials.

To analyze the low-field magnetic structure of CeSbTe, neutron powder diffraction measurements were performed. Some refinements are shown in Fig. 3D, and more detailed figures and tables with refined parameters can be found in the Supplementary Materials. As mentioned before, at 5 K, above the Néel temperature, the refinement yields the tetragonal space group $P4/nmm$, in agreement with the results from SXRD and PED. Upon cooling, additional Bragg peaks appear owing to magnetic order. These extra reflections can be indexed with a propagation vector $\mathbf{k} = (0, 0, \frac{1}{2})$, and the absence of the $(00l \pm \frac{1}{2})$ reflections clearly indicates that the spins are oriented along the c direction, matching the indications from the susceptibility data (see the Supplementary Materials for details). The magnetic structure was solved at 1.5 K with a doubling of the unit cell along c in the magnetic space group $P4/ncc$ (no. 130.432, type IV) corresponding to the mZ_1^+ irreducible representation (see Fig. 3D for a fit of the nuclear and magnetic

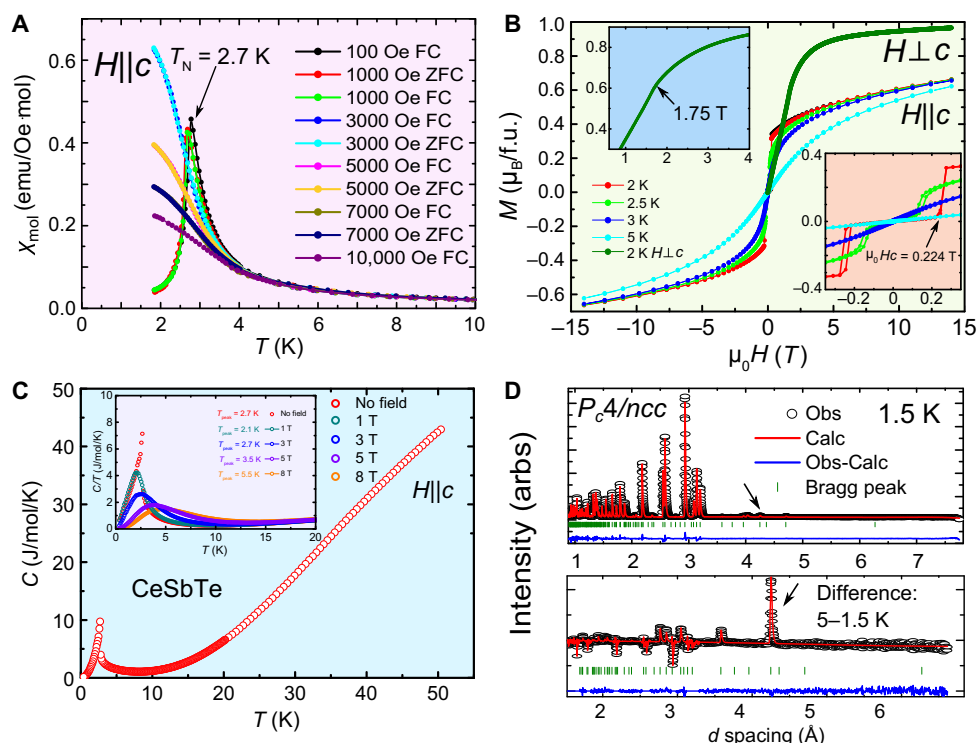


Fig. 3. Magnetic properties of CeSbTe. (A) Temperature-dependent magnetic susceptibility; different colored lines represent different applied field strengths ($H \parallel c$). (B) Field-dependent magnetic susceptibility; different colors represent different temperatures. Below T_N , a field direction-dependent magnetic transition is observed that is reached at lower field strengths for $H \parallel c$, but the saturation moment is reached faster with $H \perp c$. (C) Specific heat of CeSbTe. The magnetic transition is clearly visible at 2.7 K. The inset shows the behavior with different applied field strengths. (D) Refinement of neutron diffraction data taken at 1.5 K, below the magnetic transition. The lower panel shows the pure magnetic diffraction pattern, which was obtained by subtracting the 5-K data from the 1.5-K data. The region below the nuclear Bragg reflection was excluded from the refinement because of the irregular background caused by small changes in the cell parameters between the two temperatures. Arrows point to the main magnetic Bragg peak, indicating the doubling of the unit cell. emu, electromagnetic unit; f.u., formula unit.

contributions and the pure magnetic diffraction pattern). A drawing of the magnetic structure can be found in Fig. 4. In each Ce single layer, the spins are ferromagnetically arranged and coupled antiferromagnetically with the following layer, forming an AFM bilayer. The bilayers are then coupled antiferromagnetically with each other, which causes the doubling of the unit cell along c . Further information regarding the magnetic structure solution is given in the Supplementary Materials.

The magnetic phase diagram of CeSbTe is summarized in Fig. 4, which includes the results of the susceptibility, specific heat, and neutron diffraction measurements, measured on multiple and distinct single crystals. The transition temperatures in the susceptibility data were inferred from the derivative $d(\chi T)/dT$. There are three regions in the phase diagram: at temperatures below $T_N = 2.7$ K and $\mu_0 H_c = 0.224$ T, the spins order antiferromagnetically; above the critical field, they switch to an FM-type, fully polarized order; and above T_N and low field, the material is paramagnetic. Note that the spin-flop transition to the FM phase happens at higher field strengths if the field is aligned perpendicular to the c axis. Depending on the field alignment, the spins can be adjusted to point in different crystallographic directions.

DISCUSSION

The different possibilities of magnetic order are expected to have a significant effect on the electronic structure of CeSbTe. In the paramagnetic case, TRS is preserved, conserving the fourfold degeneracies at the nonsymmorphically protected high-symmetry points. In the AFM and

FM phases, it is broken, which usually leads to a lifting of degeneracies. In addition, in the AFM structure, there is now an antitranslation $\{1| (0, 0, \frac{1}{2})\}$ acting on the Ce atoms; thus, this phase has an additional nonsymmorphic symmetry element. Figure 5A shows the calculated band structure of the paramagnetic phase of CeSbTe. Without consideration of f -electrons and spin polarization, fourfold degenerate lines, protected by joint IS, TRS, and nonsymmorphic symmetries, exist on the boundary of the BZ, such as that along RX, similar to ZrSiS and related compounds (21, 29). These fourfold protected crossings are guaranteed by group theory to be present in the space group $P4/nmm$ (34), and their appearance in the DFT calculation confirms the accuracy of the latter in this case. At the X point, one of these crossings appears very close to the Fermi level (see the green highlight in Fig. 5C). Further fourfold degeneracies appear at M and A, but those are much further away from the Fermi level. Along ΓZ , there is a slightly tilted Dirac crossing that is protected by the fourfold rotation symmetry in the tetragonal space group $P4/nmm$.

If magnetism is included in the calculation, then the electronic structure is affected rather severely depending on the type of magnetic order and the orientation of the spins. As long as spin polarization is taken into consideration, the symmetry is reduced by breaking TRS, leading to splitting of the fourfold degenerate lines. Figure 5C shows the region around the X point, when different types of spin polarizations are included in the calculation. For complete plots of the electronic structure including spin polarization, see the Supplementary Materials. Without SOC, the nonsymmorphic symmetry $C_{2x} = \{C_{2x} | (\frac{1}{2}, 0, 0)\}$ guarantees the

double degeneracy at the X point. With SOC, each band remains twofold degenerate because $(TI)^2 = -1$, where T is TRS and I is the spatial IS. The screw \bar{C}_{2x} anticommutes with I at the X point, leading to a fourfold degeneracy (35). When an FM spin polarization is taken into account, TRS is broken and the Dirac point at X splits correspondingly. The details of the band structure are strongly dependent on the orien-

tation of the magnetization. If the spins are aligned along [001], only TRS is broken, whereas the anti-unitary combination of the nonsymmorphic symmetry \bar{C}_{2x} and time-reversal $\bar{C}_{2x}T$ is preserved. Therefore, the fourfold degeneracy is reduced to a double degeneracy at X and doubly degenerate bands for all $\mathbf{k} = (\pm\pi, k_y, k_z)$. Note that this scenario appears below 2.7 K and $\mu_0 H_c > 0.224$ T if the field is aligned along the crystallographic c axis. If the spins are aligned along [100], which is analogous to [010] in a tetragonal system, only the unitary nonsymmorphic symmetry \bar{C}_{2x} remains. A new anti-unitary symmetry $m_z T$ (where m_z is a mirror operation) is present additionally, protecting a double degeneracy along the line XR. The same symmetry appears for an FM spin orientation along the [110] direction. In the AFM phase, even if TRS is no longer a symmetry of the Schrödinger Hamiltonian, the symmetry element $\{\bar{1}|(0, 0, \frac{1}{2})\}$ squares to -1 and maps k to $-k$, such as what TRS would do in space group no. 130. This is a result from the doubled c axis in this phase. Therefore, although CeSbTe crystallizes in space group no. 129, its AFM phase behaves like a material in space group no. 130 with TRS. This causes the bands to be fourfold degenerate at X, R, and M and eightfold degenerate at A at $E_i = -4.6$ eV (see Fig. 6). We can conclude that AFM order is a possibility to create higher-order degeneracies that are associated with new types of topological phases in space groups that have previously not been considered. This considerably extends the amount of materials that can exhibit such unconventional quasi-particles. For example, we can extend this scenario to further materials crystallizing in the space group $P4/nmm$, where AFM order creates additional nonsymmorphic symmetries. Examples of further materials where eightfold band degeneracies might be realistic are LiMnAs (36), CeTe₂ (31), and LaMnGe (37). All these materials are known to crystallize in the space group $P4/nmm$

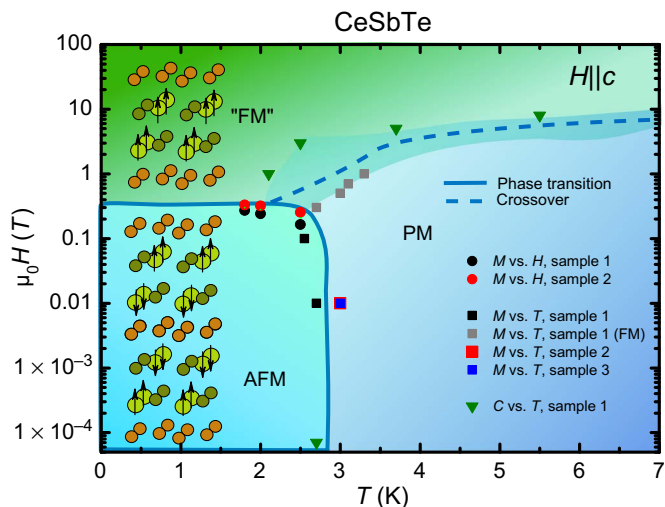


Fig. 4. Magnetic phase diagram of CeSbTe. Three different regions can be observed within a low field limit. The magnetic structures of the different phases are shown in the respective regions. Different colors indicate different samples and different symbols indicate different measurement techniques.

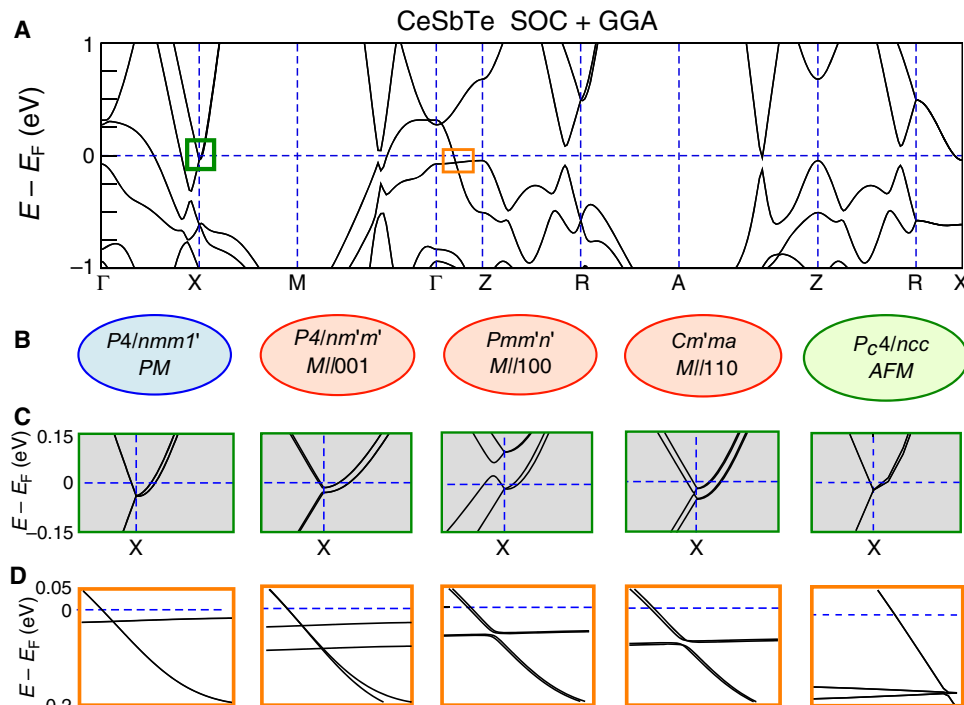


Fig. 5. Band structure of CeSbTe. (A) Calculated paramagnetic band structure including SOC. The green and orange boxes highlight the nonsymmorphic Dirac and the tilted Dirac crossing, respectively. (B) Symmetry groups of the different accessible phases (for drawings of the respective magnetic structures, see fig. S13). (C) Detailed plots of the region around the X point and how different types of magnetic order affect the electronic structure. (D) Detailed plots of the region along ΓZ and the effect of magnetic order.

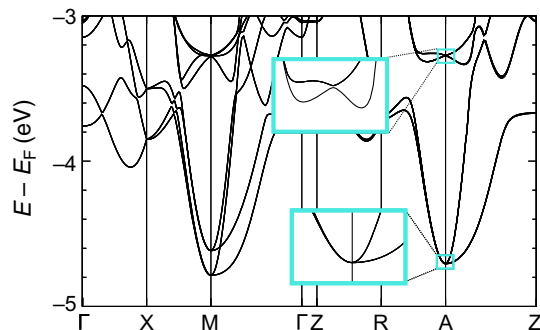


Fig. 6. Band structure of the AFM phase of CeSbTe plotted for lower energies to highlight the degeneracies at the A point. Two crossing points are highlighted, with the lower one showing a true eightfold degeneracy.

and double their c axis by adding an antitranlation symmetry operation ($\{\mathbb{1}|(0, 0, \frac{1}{2})\}$) in their AFM structure.

The changes in symmetry also affect the electronic structure away from high-symmetry points. For example, twofold degenerate Weyl points appear close to the X point if the spins are aligned along [110]. In addition, there is an effect on the tilted fourfold degenerate Dirac crossing along the ΓZ direction (Fig. 5D). In the FM phase, with spins aligned along [001], one of these bands splits, whereas the other one remains degenerate, resulting in a triply degenerate point close to the Fermi level that is composed of two different irreducible representations of $2 + 1$ dimensions along the line Λ connecting Γ and Z. Triply degenerate band crossings have also been associated with the possibility of creating double Fermi arcs at the surface (16).

CeSbTe is thus a unique material that allows access to many different magnetic groups that allow for irreducible representations in various dimensionalities. Figure S7 summarizes the accessible magnetic groups and how the system can be transformed to exhibit each symmetry. Drawings of the crystal structure of CeSbTe in each magnetic group are also shown in the same figure. The magnetic groups that are accessible in CeSbTe can be either symmorphic or nonsymmorphic, which adds to the richness of the different irreducible representations that are accessible.

To have a wider view of the rich diversity of quasi-particles that appear at the time-reversal inversion momenta (TRIMs) of the different phases of CeSbTe, we have tabulated all the dimensions of the irreducible matrix representations at these points, using the double group representations of the Bilbao Crystallographic Server (23–26), including and excluding TRS. The tabulated values can be found in table S3.

The multitude of exotic quasi-particles that can be accessed by changing the temperature or applied magnetic field should be visible in scanning tunneling microscopy (STM) experiments, where the electronic structure can be investigated by measuring quasi-particle interference. STM experiments should be very sensitive to the changes in the necessarily occurring surface electronic structure when a magnetic field is applied. Surface states related to Weyl nodes that can be controlled by a magnetic field should be identifiable by careful surface-sensitive spectroscopic techniques, despite the convolution with other bulk states.

CONCLUSION

In conclusion, we showed that the tetragonal compound CeSbTe can host many different topological features in its electronic structure,

ranging from fourfold and twofold Dirac and Weyl crossings to more exotic eightfold and threefold degeneracies. Because of the easy access to several different magnetic phases, this system is a rich playground to study the effects of symmetry breaking due to magnetic order on different types of Dirac crossings, as well as on higher-order degeneracies that result from nonsymmorphic symmetry. In particular, the AFM phase is represented by a space group of higher symmetry order, the nonsymmorphic group P_4/ncc . Because of the added symmetry elements, the material shows the same irreducible representations as materials that crystallize in space group no. 130 with TRS. As a consequence, CeSbTe displays exotic states such as eightfold degenerate new fermions. This concept can also be extended to further materials crystallizing in space group no. 129 (a much more abundant space group compared to no. 130), significantly increasing the available materials that could host new fermions. Because of the difficulty of taking ARPES spectra in the presence of a magnetic field, future investigations of CeSbTe with STM are of high interest.

MATERIALS AND METHODS

Single crystals were grown with iodine vapor transport. The crystal structure was solved with SXRD, neutron diffraction, and electron diffraction (see the Supplementary Materials for details). Magnetic measurements were performed on a magnetic property measurement system–XL and a physical property measurement system (PPMS) equipped with a vibrating sample magnetometer option from Quantum Design. Specific heat measurements were performed on a PPMS from Quantum Design. Powder neutron diffraction data were collected on the WISH instrument at ISIS, Harwell Oxford (see the Supplementary Materials for details) (38). For ARPES measurements, crystals were cleaved and measured in ultrahigh vacuum (low 10^{-10} mbar range). Spectra were recorded with the 1^2 -ARPES experiment installed at the UE112-PGM2a beamline at BESSY-II in Berlin. The spectra were taken at room temperature. DFT calculations were performed using the augmented plane-wave method, as implemented in the Vienna ab initio Simulation Package (39). Because of the presence of Ce- f electrons, we have considered the exchange-correlation energy by the DFT + U method, with $U = 6$ eV (or $U = 5$ eV) added to the Ce atoms (40), reproducing the experimentally measured magnetic moment and the experimental energy of the Ce $4f$ states. To model the paramagnetic phase, we used a Ce-pseudopotential in which the $4f$ electron was placed in the core to model the Ce $^{3+}$ valence. For the surface slab calculations, a slab containing five unit cells was used. All the electronic structures were calculated based on experimental lattice constants, including SOC.

SUPPLEMENTARY MATERIALS

Supplementary material for this article is available at <http://advances.sciencemag.org/cgi/content/full/4/2/eaar2317/DC1>

Supplementary Text

fig. S1. Electron diffraction on CeSbTe.

fig. S2. Analysis of neutron powder diffraction data.

fig. S3. Refinement of the pure magnetic Bragg peaks, obtained by subtraction of the 5-K data from the 1.5-K data with respect to the two possible different magnetic structures.

fig. S4. Energy dispersions of CeSbTe along high-symmetry lines.

fig. S5. Additional ARPES measurements on CeSbTe.

fig. S6. Additional magnetic susceptibility and specific heat data.

fig. S7. Accessible magnetic subgroups discussed in this paper.

table S1. Crystallographic data and details of data collection for single-crystal x-ray and low-temperature neutron diffraction.

table S2. Position coordinates and thermal displacement parameters for paramagnetic (top) and AFM (bottom) CeSbTe.
table S3. Possible dimensions of the irreducible representations at each TRIM and along certain high-symmetry lines of different phases of CeSbTe.

REFERENCES AND NOTES

- S. Borisenko, Q. Gibson, D. Evtushinsky, V. Zabolotnyy, B. Büchner, R. J. Cava, Experimental realization of a three-dimensional Dirac semimetal. *Phys. Rev. Lett.* **113**, 027603 (2014).
- Z. K. Liu, B. Zhou, Y. Zhang, Z. J. Wang, H. M. Weng, D. Prabhakaran, S.-K. Mo, Z. X. Shen, Z. Fang, X. Dai, Z. Hussain, Y. L. Chen, Discovery of a three-dimensional topological Dirac semimetal, Na₃Bi. *Science* **343**, 864–867 (2014).
- P. J. W. Moll, N. L. Nair, T. Helm, A. C. Potter, I. Kimchi, A. Vishwanath, J. G. Analytis, Transport evidence for Fermi-arc-mediated chirality transfer in the Dirac semimetal Cd₃As₂. *Nature* **535**, 266–270 (2016).
- T. Liang, Q. Gibson, M. N. Ali, M. Liu, R. J. Cava, N. P. Ong, Ultrahigh mobility and giant magnetoresistance in the Dirac semimetal Cd₃As₂. *Nat. Mater.* **14**, 280–284 (2015).
- J. Xiong, S. K. Kushwaha, T. Liang, J. W. Krizan, M. Hirschberger, W. Wang, R. J. Cava, N. P. Ong, Evidence for the chiral anomaly in the Dirac semimetal Na₃Bi. *Science* **350**, 413–416 (2015).
- Y. Sun, Y. Zhang, C. Felser, B. Yan, Strong intrinsic spin Hall effect in the TaAs family of Weyl semimetals. *Phys. Rev. Lett.* **117**, 146403 (2016).
- L. Šmejkal, J. Železný, J. Sinova, T. Jungwirth, Electric control of Dirac quasiparticles by spin-orbit torque in an antiferromagnet. *Phys. Rev. Lett.* **118**, 106402 (2017).
- X. Wan, A. M. Turner, A. Vishwanath, S. Y. Savrasov, Topological semimetal and Fermi-arc surface states in the electronic structure of pyrochlore iridates. *Phys. Rev. B* **83**, 205101 (2011).
- S.-Y. Xu, I. Belopolski, N. Alidoust, M. Neupane, G. Bian, C. Zhang, R. Sankar, G. Chang, Z. Yuan, C.-C. Lee, S.-M. Huang, H. Zheng, J. Ma, D. S. Sanchez, B. Wang, A. Bansil, F. Chou, P. P. Shibayev, H. Lin, S. Jia, M. Z. Hasan, Discovery of a Weyl fermion semimetal and topological Fermi arcs. *Science* **349**, 613–617 (2015).
- B. Lv, N. Xu, H. M. Weng, J. Z. Ma, P. Richard, X. C. Huang, L. X. Zhao, G. F. Chen, C. E. Matt, F. Bisti, V. N. Strocov, J. Mesot, Z. Fang, X. Dai, T. Qian, M. Shi, H. Ding, Observation of Weyl nodes in TaAs. *Nat. Phys.* **11**, 724–727 (2015).
- M. Hirschberger, S. Kushwaha, Z. Wang, Q. Gibson, S. Liang, C. A. Belvin, B. A. Bernevig, R. J. Cava, N. P. Ong, The chiral anomaly and thermopower of Weyl fermions in the half-Heusler GdPtBi. *Nat. Mater.* **15**, 1161–1165 (2016).
- Z. Wang, M. G. Vergniory, S. Kushwaha, M. Hirschberger, E. V. Chulkov, A. Ernst, N. P. Ong, R. J. Cava, B. A. Bernevig, Time-reversal-breaking Weyl fermions in magnetic Heusler alloys. *Phys. Rev. Lett.* **117**, 236401 (2016).
- P. Tang, Q. Zhou, G. Xu, S.-C. Zhang, Dirac fermions in an antiferromagnetic semimetal. *Nat. Phys.* **2**, 1100–1104 (2016).
- E. Emmanouilidou, H. Cao, P. Tang, X. Gui, C. Hu, B. Shen, J. Wu, S.-C. Zhang, W. Xie, N. Ni, Magnetic order induces symmetry breaking in the single-crystalline orthorhombic CuMnAs semimetal. *Phys. Rev. B* **96**, 224405 (2017).
- S. M. Young, S. Zaheer, J. C. Y. Teo, C. L. Kane, E. J. Mele, A. M. Rappe, Dirac semimetal in three dimensions. *Phys. Rev. Lett.* **108**, 140405 (2012).
- B. Bradlyn, J. Cano, Z. Wang, M. G. Vergniory, C. Felser, R. J. Cava, B. A. Bernevig, Beyond Dirac and Weyl fermions: Unconventional quasiparticles in conventional crystals. *Science* **353**, aaf5037 (2016).
- B. J. Wieder, Y. Kim, A. M. Rappe, C. L. Kane, Double Dirac semimetals in three dimensions. *Phys. Rev. Lett.* **116**, 186402 (2016).
- H. Watanabe, H. C. Po, M. P. Zaletel, A. Vishwanath, Filling-enforced gaplessness in band structures of the 230 space groups. *Phys. Rev. Lett.* **117**, 096404 (2016).
- A. Topp, J. M. Lippmann, A. Varykhalov, V. Duppel, B. V. Lotsch, C. R. Ast, L. M. Schoop, Non-symmorphic band degeneracy at the Fermi level in ZrSiTe. *New J. Phys.* **18**, 125014 (2016).
- L. M. Schoop, M. N. Ali, C. Straßer, A. Topp, A. Varykhalov, D. Marchenko, V. Duppel, S. S. P. Parkin, B. V. Lotsch, C. R. Ast, Dirac cone protected by non-symmorphic symmetry and three-dimensional Dirac line node in ZrSiS. *Nat. Commun.* **7**, 11696 (2016).
- C. Chen, X. Xu, J. Jiang, S.-C. Wu, Y. P. Qi, L. X. Yang, M. X. Wang, Y. Sun, N. B. M. Schröter, H. F. Yang, L. M. Schoop, Y. Y. Lv, J. Zhou, Y. B. Chen, S. H. Yao, M. H. Lu, Y. F. Chen, C. Felser, B. H. Yan, Z. K. Liu, Y. L. Chen, Dirac line nodes and effect of spin-orbit coupling in the nonsymmorphic critical semimetals M SiS (M = Hf, Zr). *Phys. Rev. B* **95**, 125126 (2017).
- H. Watanabe, H. C. Po, A. Vishwanath, Structure and topology of band structures in the 1651 magnetic space groups. arXiv preprint arXiv:1707.01903 (2017).
- M. I. Aroyo, J. M. Perez-Mato, D. Orobengoa, E. Tasci, G. de la Flor, A. Kirov, Crystallography online: Bilbao crystallographic server. *Bulg. Chem. Commun.* **43**, 183–197 (2011).
- M. I. Aroyo, J. M. Perez-Mato, C. Capillas, E. Kroumova, S. Ivantchev, G. Madariaga, A. Kirov, H. Wondratschek, Bilbao Crystallographic Server I: Databases and crystallographic computing programs. *Zeitschrift für Kristallographie* **221**, 15–27 (2006).
- M. I. Aroyo, A. Kirov, C. Capillas, J. M. Perez-Mato, H. Wondratschek, Bilbao Crystallographic Server. II. Representations of crystallographic point groups and space groups. *Acta Crystallogr. A* **62**, 115–128 (2006).
- J. M. Perez-Mato, S. V. Gallego, E. S. Tasci, L. Elcoro, G. de la Flor, M. I. Aroyo, Symmetry-based computational tools for magnetic crystallography. *Annu. Rev. Mat. Res.* **45**, 217–248 (2015).
- Y. C. Wang, K. M. Poduska, R. Hoffmann, F. J. DiSalvo, Structure and physical properties of CeSbTe. *J. Alloys Compd.* **314**, 132–139 (2001).
- Q. Xu, Z. Song, S. Nie, H. Weng, Z. Fang, X. Dai, Two-dimensional oxide topological insulator with iron-pnictide superconductor LiFeAs structure. *Phys. Rev. B* **92**, 205310 (2015).
- A. Topp, R. Queiroz, A. Grüneis, L. Mückler, A. Rost, A. Varykhalov, D. Marchenko, M. Krivenkov, F. Rodolakis, J. McChesney, B. V. Lotsch, L. M. Schoop, C. R. Ast, Surface floating 2D bands in layered nonsymmorphic semimetals: ZrSiS and related compounds. *Phys. Rev. X* **7**, 041073 (2017).
- D. W. Lynch, J. H. Weaver, Photoemission of Ce and its compounds. *Handb. Phys. Chem. Rare Earths* **10**, 231–300 (1987).
- J.-G. Park, I. P. Swainson, W. J. L. Buyers, M. H. Jung, Y. S. Kwon, Influence of field-dependent magnetic structure of CeTe₂ on its resistivity. *Phys. B Condens. Matter* **241–243**, 684–686 (1997).
- K.-W. Chen, Y. Lai, Y.-C. Chiu, S. Steven, T. Besara, D. Graf, T. Siegrist, T. E. Albrecht-Schmitt, L. Balicas, R. E. Baumbach, Possible devil's staircase in the Kondo lattice CeSbSe. *Phys. Rev. B* **96**, 014421 (2017).
- F. von Rohr, A. Krzton-Maziopa, V. Pomjakushin, H. Grundmann, Z. Guguchia, W. Schnick, A. Schilling, Field-induced transition of the magnetic ground state from A-type antiferromagnetic to ferromagnetic order in CsCo₂Se₂. *J. Phys. Condens. Matter* **28**, 276001 (2016).
- L. Elcoro, B. Bradlyn, Z. Wang, M. G. Vergniory, J. Cano, C. Felser, B. A. Bernevig, D. Orobengoa, G. de la Flor, M. I. Aroyo, Double crystallographic groups and their representations on the Bilbao Crystallographic Server. *J. Appl. Cryst.* **50**, 1457–1477 (2017).
- S. M. Young, C. L. Kane, Dirac semimetals in two dimensions. *Phys. Rev. Lett.* **115**, 126803 (2015).
- A. Beleanu, J. Kiss, G. Kreiner, C. Köhler, L. Mückler, W. Schnelle, U. Burkhardt, S. Chadov, S. Medvedev, D. Ebke, C. Felser, G. Cordier, B. Albert, A. Hoser, F. Bernardi, T. I. Larkin, D. Pröpper, A. V. Boris, B. Keimer, Large resistivity change and phase transition in the antiferromagnetic semiconductors LiMnAs and LaOMnAs. *Phys. Rev. B* **88**, 184429 (2013).
- R. Welter, G. Venturini, E. Ressouche, B. Malaman, Crystallographic data and magnetic properties of new CeFeSi-type RMnGe compounds (R = La - Sm) studied by magnetization and neutron diffraction measurements. *J. Alloys Compd.* **228**, 59–74 (1995).
- L. C. Chapon, P. Manuel, P. G. Radaelli, C. Benson, L. Perrott, S. Ansell, N. J. Rhodes, D. Raspino, D. Duxbury, E. Spill, J. Norris, Wish: The new powder and single crystal magnetic diffractometer on the second target station. *Neutron News* **22**, 22–25 (2011).
- G. Kresse, J. Furthmüller, Efficiency of ab-initio total energy calculations for metals and semiconductors using a plane-wave basis set. *Comput. Mater. Sci.* **6**, 15–50 (1996).
- S. L. Dudarev, G. A. Botton, S. Y. Savrasov, C. J. Humphreys, A. P. Sutton, Electron-energy-loss spectra and the structural stability of nickel oxide: An LSDA+U study. *Phys. Rev. B* **57**, 1505 (1998).

Acknowledgments: We thank R. Eger for the single-crystal diffraction measurements.

Funding: We acknowledge the financial support from the Max Planck Society, the Nanosystems Initiative Munich, and the Center for Nanosciences. L.M.S. acknowledges the financial support from the Minerva Fast Track Fellowship. M.G.V. was supported by the FIS2016-75862-P national projects of the Ministry of Economy and Competitiveness, Spain. This work was partially supported by the Deutsche Forschungsgemeinschaft within the proposal Dirac materials in square lattice compounds under proposal SCHO 1730/1-1. The authors acknowledge the Science and Technology Facility Council for the provision of neutron beamtime at the ISIS facility (UK). **Author contributions:** L.M.S. initiated the project and performed initial calculations of the bulk electronic structure, thus identifying CeSbTe as a compound that could combine topology and magnetism. L.M.S. and J.L. grew the crystals and performed the magnetic susceptibility measurements together with A.W.R. A.T., S.S., A.V., and M.K. measured and analyzed ARPES spectra at BESSY. A.T., F.O., and P.M. performed neutron measurements at WISH. F.O. and P.M. analyzed the neutron data and solved the magnetic structure. L.M., B.Y., Y.S., and M.G.V. performed the DFT calculations and wrote the theoretical part of the manuscript. M.G.V. performed the group theory

analysis with input from F.O. V.D. investigated the samples using transmission electron microscopy. R.K.K. performed the specific heat measurements, repeated some of the susceptibility measurements, and fitted the CEF. A.W.R., L.M.S., and R.K.K. interpreted the magnetic properties. L.M.S., A.W.R., and C.R.A. helped interpret the ARPES data. C.R.A. and B.V.L. supervised the research. All authors discussed the results of the paper and contributed to the writing of the manuscript. **Competing interests:** The authors declare that they have no competing interests. **Data and materials availability:** All data needed to evaluate the conclusions of the paper are present in the paper and/or the Supplementary Materials. Additional data related to this paper may be requested from the authors.

Submitted 16 October 2017

Accepted 23 January 2018

Published 23 February 2018

10.1126/sciadv.aar2317

Citation: L. M. Schoop, A. Topp, J. Lippmann, F. Orlandi, L. Mühler, M. G. Vergniory, Y. Sun, A. W. Rost, V. Duppel, M. Krivenkov, S. Sheoran, P. Manuel, A. Varykhalov, B. Yan, R. K. Kremer, C. R. Ast, B. V. Lotsch, Tunable Weyl and Dirac states in the nonsymmorphic compound CeSbTe. *Sci. Adv.* **4**, eaar2317 (2018).